Ultra-high resolution Fourier domain optical coherence tomography for old master paintings

C. S. Cheung,[1] M. Spring,[2] and H. Liang[1,*]

[1]*School of Science and Technology, Nottingham Trent University, Nottingham NG11 8NS, UK*
[2]*Scientific Department, National Gallery, London WC2N 5DN, UK*
[*]*Haida.Liang@ntu.ac.uk*

Abstract: In the last 10 years, Optical Coherence Tomography (OCT) has been successfully applied to art conservation, history and archaeology. OCT has the potential to become a routine non-invasive tool in museums allowing cross-section imaging anywhere on an intact object where there are no other methods of obtaining subsurface information. While current commercial OCTs have shown potential in this field, they are still limited in depth resolution (> 4 μm in paint and varnish) compared to conventional microscopic examination of sampled paint cross-sections (~ 1 μm). An ultra-high resolution fiber-based Fourier domain optical coherence tomography system with a constant axial resolution of 1.2 μm in varnish or paint throughout a depth range of 1.5 mm has been developed. While Fourier domain OCT of similar resolution has been demonstrated recently, the sensitivity roll-off of some of these systems are still significant. In contrast, this current system achieved a sensitivity roll-off that is less than 2 dB over a 1.2 mm depth range with an incident power of ~ 1 mW on the sample. The high resolution and sensitivity of the system makes it convenient to image thin varnish and glaze layers with unprecedented contrast. The non-invasive 'virtual' cross-section images obtained with the system show the thin varnish layers with similar resolution in the depth direction but superior clarity in the layer interfaces when compared with conventional optical microscope images of actual paint sample cross-sections obtained micro-destructively.

OCIS codes: (110.4500) Optical coherence tomography; (120.3180) Interferometry; (120.4290) Nondestructive testing.

References and links

1. D. Huang, E. A. Swanson, C. P. Lin, J. S. Schuman, W. G. Stinson, W. Chang, M. R. Hee, T. Flotte, K. Gregory, C. A. Puliafito, and J. G. Fujimoto, "Optical coherence tomography," Science **254**(5035), 1178–1181 (1991).
2. A. Fercher, C. Hitzenberger, G. Kamp, and S. El-Zaiat, "Measurement of intraocular distances by backscattering spectral interferometry," Opt. Commun. **117**(1-2), 43–48 (1995).
3. D. Stifter, "Beyond biomedicine: a review of alternative applications and developments for optical coherence tomography," Appl. Phys. B **88**(3), 337–357 (2007).
4. P. Targowski and M. Iwanicka, "Optical Coherence Tomography for structural examination of cultural heritage objects and monitoring of restoration processes – a review," Appl. Phys., A Mater. Sci. Process. **106**, 265–277 (2012).
5. H. Liang, B. Peric, M. Hughes, A. Podoleanu, M. Spring, and S. Roehrs, "Optical Coherence Tomography in Archaeology and Conservation Science – a new emerging field," Proc. SPIE **7139**, 713915 (2008).
6. H. Liang, M. G. Cid, R. G. Cucu, G. M. Dobre, A. Podoleanu, J. Pedro, and D. Saunders, "En-face Optical Coherence Tomography - a novel application of non-invasive imaging to art conservation," Opt. Express **13**(16), 6133–6144 (2005).
7. S. Lawman and H. Liang, "High precision dynamic multi-interface profilometry with optical coherence tomography," Appl. Opt. **50**(32), 6039–6048 (2011).
8. P. Targowski, R. Ostrowski, M. Marczak, M. Sylwestrzak, and E. A. Kwiatkowska, "Picosecond laser ablation system with process control by optical coherence tomography," Proc. SPIE **7391**, 73910G (2009).

9. P. Targowski, M. Góra, T. Bajraszewski, M. Szkulmowski, B. Rouba, T. Łękawa-Wysłouch, and L. Tymińska-Widmer, "Optical coherence tomography for tracking canvas deformation," Laser Chem. **2006**, 93658 (2006).
10. L. Vabre, A. Dubois, and A. C. Boccara, "Thermal-light full-field optical coherence tomography," Opt. Lett. **27**(7), 530–532 (2002).
11. G. Latour, J. P. Echard, B. Soulier, I. Emond, S. Vaiedelich, and M. Elias, "Structural and optical properties of wood and wood finishes studied using optical coherence tomography: application to an 18th century Italian violin," Appl. Opt. **48**(33), 6485–6491 (2009).
12. H. Liang, R. Lange, B. Peric, and M. Spring, "Optimum spectral window for imaging of art with optical coherence tomography," Appl. Phys. B **111**(4), 589–602 (2013).
13. B. Povazay, K. Bizheva, A. Unterhuber, B. Hermann, H. Sattmann, A. F. Fercher, W. Drexler, A. Apolonski, W. J. Wadsworth, J. C. Knight, P. S. Russell, M. Vetterlein, and E. Scherzer, "Submicrometer axial resolution optical coherence tomography," Opt. Lett. **27**(20), 1800–1802 (2002).
14. K. Bizheva, B. Považay, B. Hermann, H. Sattmann, W. Drexler, M. Mei, R. Holzwarth, T. Hoelzenbein, V. Wacheck, and H. Pehamberger, "Compact, broad-bandwidth fiber laser for sub-2-microm axial resolution optical coherence tomography in the 1300-nm wavelength region," Opt. Lett. **28**(9), 707–709 (2003).
15. W. Drexler, "Ultrahigh-resolution optical coherence tomography," J. Biomed. Opt. **9**(1), 47–74 (2004).
16. R. Leitgeb, C. Hitzenberger, and A. Fercher, "Performance of fourier domain vs. time domain optical coherence tomography," Opt. Express **11**(8), 889–894 (2003).
17. J. F. de Boer, B. Cense, B. H. Park, M. C. Pierce, G. J. Tearney, and B. E. Bouma, "Improved signal-to-noise ratio in spectral-domain compared with time-domain optical coherence tomography," Opt. Lett. **28**(21), 2067–2069 (2003).
18. M. A. Choma, M. V. Sarunic, C. H. Yang, and J. A. Izatt, "Sensitivity advantage of swept source and Fourier domain optical coherence tomography," Opt. Express **11**(18), 2183–2189 (2003).
19. M. Wojtkowski, R. Leitgeb, A. Kowalczyk, T. Bajraszewski, and A. F. Fercher, "In vivo human retinal imaging by Fourier domain optical coherence tomography," J. Biomed. Opt. **7**(3), 457–463 (2002).
20. M. Wojtkowski, V. Srinivasan, T. Ko, J. Fujimoto, A. Kowalczyk, and J. Duker, "Ultrahigh-resolution, high-speed, Fourier domain optical coherence tomography and methods for dispersion compensation," Opt. Express **12**(11), 2404–2422 (2004).
21. R. Leitgeb, W. Drexler, A. Unterhuber, B. Hermann, T. Bajraszewski, T. Le, A. Stingl, and A. Fercher, "Ultrahigh resolution Fourier domain optical coherence tomography," Opt. Express **12**(10), 2156–2165 (2004).
22. B. Cense, N. Nassif, T. Chen, M. Pierce, S. H. Yun, B. Park, B. Bouma, G. Tearney, and J. de Boer, "Ultrahigh-resolution high-speed retinal imaging using spectral-domain optical coherence tomography," Opt. Express **12**(11), 2435–2447 (2004).
23. S. Kray, F. Spöler, M. Först, and H. Kurz, "High-resolution simultaneous dual-band spectral domain optical coherence tomography," Opt. Lett. **34**(13), 1970–1972 (2009).
24. V. J. Srinivasan, Y. Chen, J. S. Duker, and J. G. Fujimoto, "In Vivo Functional Imaging of Intrinsic Scattering Changes in the Human Retina with High-Speed Ultrahigh Resolution OCT," Opt. Express **17**(5), 3861–3877 (2009).
25. B. Cense, E. Koperda, J. M. Brown, O. P. Kocaoglu, W. Gao, R. S. Jonnal, and D. T. Miller, "Volumetric retinal imaging with ultrahigh-resolution spectral-domain optical coherence tomography and adaptive optics using two broadband light sources," Opt. Express **17**(5), 4095–4111 (2009).
26. P. Cimalla, J. Walther, M. Mehner, M. Cuevas, and E. Koch, "Simultaneous dual-band optical coherence tomography in the spectral domain for high resolution in vivo imaging," Opt. Express **17**(22), 19486–19500 (2009).
27. E. Götzinger, B. Baumann, M. Pircher, and C. K. Hitzenberger, "Polarization maintaining fiber based ultra-high resolution spectral domain polarization sensitive optical coherence tomography," Opt. Express **17**(25), 22704–22717 (2009).
28. Z. Zhi, J. Qin, L. An, and R. K. Wang, "Supercontinuum light source enables in vivo optical microangiography of capillary vessels within tissue beds," Opt. Lett. **36**(16), 3169–3171 (2011).
29. B. Potsaid, I. Gorczynska, V. J. Srinivasan, Y. Chen, J. Jiang, A. Cable, and J. G. Fujimoto, "Ultrahigh speed Spectral / Fourier domain OCT ophthalmic imaging at 70,000 to 312,500 axial scans per second," Opt. Express **16**(19), 15149–15169 (2008).
30. R. Yadav, K. S. Lee, J. P. Rolland, J. M. Zavislan, J. V. Aquavella, and G. Yoon, "Micrometer axial resolution OCT for corneal imaging," Biomed. Opt. Express **2**(11), 3037–3046 (2011).
31. L. Liu, J. A. Gardecki, S. K. Nadkarni, J. D. Toussaint, Y. Yagi, B. E. Bouma, and G. J. Tearney, "Imaging the subcellular structure of human coronary atherosclerosis using micro-optical coherence tomography," Nat. Med. **17**(8), 1010–1014 (2011).
32. C. S. Cheung and H. Liang, "Ultra-high resolution Fourier domain optical coherence tomography for resolving thin layers in painted works of art," Proc. SPIE **8790**, 87900M (2013).
33. M. Mujat, B. H. Park, B. Cense, T. C. Chen, and J. F. de Boer, "Autocalibration of spectral-domain optical coherence tomography spectrometers for in vivo quantitative retinal nerve fiber layer birefringence determination," J. Biomed. Opt. **12**(4), 041205 (2007).
34. W. J. Brown, S. Kim, and A. Wax, "Noise characterization of supercontinuum sources for low-coherence interferometry applications," J. Opt. Soc. Am. A **31**(12), 2703–2710 (2014).

35. C. S. Cheung, J. M. O. Daniels, M. Tokurakawa, W. A. Clarkson Wa, and H. Liang, "Optical coherence tomography in the two-micron wavelength regime for paint and other high opacity material," Opt. Lett. **39**, 6509–6512 (2014).
36. C. S. Cheung, J. M. O. Daniels, M. Tokurakawa, W. A. Clarkson Wa, and H. Liang, "High resolution Fourier domain optical coherence tomography in the 2 μm wavelength range using a broadband supercontinuum source," Opt. Express **23**(3), 1992–2001 (2015).

1. Introduction

Optical Coherence Tomography (OCT) is a non-invasive, non-contact 3D imaging technique based on low coherence interferometry [1]. It uses a fast scanning Michelson interferometer with a broadband laser source to allow the visualization of subsurface microstructure. The first OCT systems were time domain, where the reference mirror scans to produce the interference fringes [1]. Fercher et al. [2] proposed the first Fourier domain OCT system, where the interference fringes were collected through a spectrometer with a fixed reference mirror. Initially designed for *in vivo* imaging of the eye, the OCT technique has found applications beyond the biomedical field [3]. The non-invasive nature of OCT imaging makes it particularly attractive to museums and galleries for two reasons: i) it allows probing of the object over a large scale in any area of choice, and can give a more representative view than if the subsurface structure is investigated only with micro-samples of paint sub-millimeter in size and ii) it can reduce the need to take samples from an artifact. Conservation ethics not only limit the amount of sample but also the site from which they can be taken, depending on the type of object as well as its condition. For example, for historical western European paintings, sampling must be limited to edges and around cracks or damaged areas of the paintings. In the last 10 years, OCT has been successfully applied to the examination of historical objects for conservation, art history and archaeological studies [4,5]. It has been used to examine the stratigraphy of paint and varnish layers of historical paintings and shown to be the most sensitive technique for revealing preparatory drawings beneath paint layers owing to its high dynamic range and depth selection capabilities [6]. It has also been used for dynamic monitoring of the wetting and drying of different varnishes [7], varnish removal using solvents [5], real time laser ablation of varnish layers [8] and tracking of canvas deformation due to environmental changes [9]. While OCT has been successfully applied to the examination of the stratigraphy of paintings, the depth resolution of OCTs used in these applications still cannot match the micro-destructive method of optical microscopic examination of paint samples prepared as cross-sections (typical resolution ~1 μm). It is known that some varnish and paint layers can be as thin as a few microns. The depth resolution of commercial OCT systems is rarely better than 6 μm in air (or 4 μm in varnish). A depth resolution close to 1 μm is needed to resolve the thinnest varnish and paint layers. The depth resolution of OCT is given by $\Delta z \propto \lambda_0^2 / \Delta \lambda$ where $\Delta \lambda$ is the bandwidth and λ_0 is the central wavelength, hence ultra-wide bandwidth light source at short central wavelength is needed for increased depth resolution.

Initially full field time domain OCTs using white light sources in the visible part of the spectrum were constructed to reach high depth resolutions of ~1 μm [10,11], however, they have low sensitivity compared with systems using laser sources and have very limited depth penetration as most paints are opaque in the visible range [12].

The first generation ultra-high resolution (UHR) OCT around 1 μm axial resolution was based on time domain systems [13,14] and until recently time domain OCT was considered the best modality for UHR OCT [15]. However, given the much improved sensitivity and speed of Fourier domain OCT (FDOCT) over time domain OCT [16–18], there was the incentive to develop FDOCT systems for ultra-high resolution imaging. The development of ultra-high resolution FDOCT is challenging because the spectrometer needs to cover a broad spectral range to give high axial resolution but at the same time it needs to be of high spectral resolution to maintain high sensitivity and high axial resolution over a large depth range. The fringe period decreases with increased depth and hence at large depth when the fringe period

becomes smaller than the spectral resolution, the fringes will be washed out resulting in a decrease in signal with increasing depth. For a given wavelength range coverage, the spectral resolution is affected by the number of pixels in the detector and the size of the focused spot on the detector. The fringe wash out will be non-uniform over the wavelength range unless the spectral resolution is constant in $k\left(=\dfrac{2\pi}{\lambda}\right)$ For example, in the case where spectral resolution is limited by pixel sampling which is not constant in k, there will also be a broadening of the axial resolution as a function of depth [19].

Until recently, FDOCT using ultra-broad band sources only managed to achieve axial resolutions of a few microns in biological tissues [20–29]. Recent availability of commercial turn-key ultra-broad band supercontinuum sources has enabled < 2 μm axial resolution (in air) for Fourier domain OCTs [30,31]. Using a Leukos supercontinuum source, Yadav et al. [30] demonstrated a FDOCT with ~1.1 μm axial resolution in tissue, but despite using a detector array with 8160 pixels the sensitivity roll-off with depth was 21 dB over the 0.16 to 1 mm depth range. Using a Fianium supercontinuum source, Liu et al. [31] developed a FDOCT with ~1 μm axial resolution in tissue but again with a limited depth range of 0.5 mm. The depth of penetration can be limited by either the instrumental depth range or the opacity of the material. The optical properties of materials encountered in cultural heritage are heterogeneous and hence it is necessary to have a large instrumental depth range to allow for the variety of material opacities in addition to the wide range of surface undulation and thickness.

In this paper, we describe a fiber-based ultra-high resolution FDOCT system that not only has an ultra-high axial resolution of ~1.2 μm (in varnish and paint) over a depth range of 1.5 mm but also a sensitivity roll-off <2 dB (due to the spectrometer resolution) throughout a depth range of 1.2 mm.

2. Instrumentation

2.1 Instrument design

The OCT system uses a commercial supercontinuum broadband laser source from NKT (SuperK Versa). The output of the light source is split into two wavelength regions (wavelength below and above 1064 nm). The output centered at 810 nm is spectral shaped to an approximate Gaussian with FWHM bandwidth of ~200 nm. A fiber based Michelson interferometer is configured using a Thorlabs FC632-50B-APC fiber coupler with a cutoff wavelength below 600 nm (Fig. 1). The output interferometric signal is collimated with a 50 mm focal length parabolic mirror and then dispersed using a 1200 lines/mm volume holographic grating (Wasatch Photonics). Lens-based collimators suffer from chromatic aberration especially for broadband operation and will inevitably spectral shape the transmitted light and reduce the bandwidth and hence the axial resolution. Therefore for ultra-high resolution OCT it is best to use reflective optics where possible. To ensure a small focused spot on the detector, it is necessary to have a wide collimated beam at the grating. The dispersed light between 600 and 1000 nm is focused onto the 40 mm wide detector with 4096 pixels and pixel size of 10×10 μm^2 (e2V AViiVA 4010 EM4 with a camera link frame grabber NI PCIe-1433) using a large format camera lens (Zeiss 85mm f/1.4 with anti-reflection coating in the near infrared). The camera is 12 bit and has a full well capacity of 117 500 electrons. A maximum gain of 15.8 e/ADU (electrons per analog-to-digital units) was used to maximize the dynamic range while minimizing non-linearity in response (~0.04%). The camera has a maximum line rate of 37.14 kHz and read noise of < 32 electrons or 2 ADU. The dark current is negligible for the short integration times (<50 μs) employed in our applications. A dispersion compensation glass was placed in the reference arm and adjusted to minimize dispersion. A preliminary report on the system is given in a conference proceeding [32].
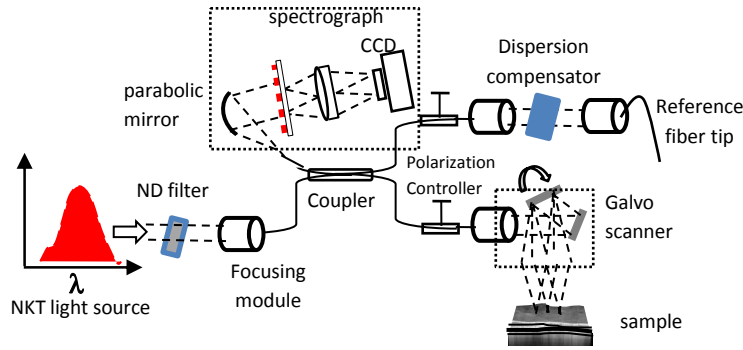
Fig. 1. Experimental setup of the ultra-high resolution 810 nm spectral domain OCT using the NKT supercontinuum light source with a 1200 l/mm grating, a 4096 pixels linear CCD detector array.

2.2 Calibration and image processing

Traditional wavelength calibration of FDOCT spectrograph is performed by imaging a mirror at one or two different depth positions and optimize for either maximum OCT signal or minimum width of depth profile at the interface [33]. For a single reflecting surface in the sample arm, a perfect sinusoid is expected in k-space and the wavelength assignment can be adjusted to match as closely as possible to a sinusoid. However, the solution is degenerate and does not independently constrain the central wavelength and the wavelength range covered by the detector. Ultra-high resolution OCT requires greater accuracy in wavelength calibration over a broad spectral range. An incorrect wavelength calibration can result in broadening of the axial resolution and an increase of axial resolution with depth. Yadav et al [20] used theoretical optical modeling to improve the spectral calibration accuracy but the verification was performed using laser line filters which are likely to have bandwidth greater than the resolution of the spectrograph. Calibration of high resolution spectrographs is commonly performed in spectroscopy using standard narrow spectral line emission from calibration lamps. Here we use 31 standard lines from Neon and Argon lamps (Ocean Optics) spanning the wavelength range of 638 nm – 912 nm for calibration. The pixel position versus wavelength data is fitted with the grating equation with focal length of the lens, grating angle of incidence and wavelength of the central pixel as free parameters or fitted with a 5th order polynomial. The rms of the fit was ~0.077 nm for the grating equation and ~0.026 nm for the 5th order polynomial (Fig. 2). It was therefore decided that the 5th order polynomial was to be used as it gave a better fit. The grating equation is a model for an ideal system that is free from aberration and is perfectly aligned. Therefore, the grating equation fit gives a diagnostic of the instrument which can help the instrument adjustment and optimization process.

The calibrated spectrum is converted into k-space and re-sampled into ~7538 equal k intervals using the minimum δk (corresponding to the pixel interval at the longest wavelength) and zero padded to 2^{14} pixels before performing a FFT to produce the depth profile. By using the minimum δk for resampling, the imaging depth is maximized. The alias free depth range is given by the pixel sampling as $\lambda^2 / 4\delta\lambda$. The pixel sampling resolution in this case is ~0.0845 nm and hence aliasing starts to affect the fringes at the short wavelength end at a depth of ~1.2 mm and affects the fringes in the entire wavelength range at a depth of 2.8 mm. In order to remove system artifacts due to inter-reflection within the system, an average of 500 background spectra taken without a sample is subtracted from all spectra. A Hann window can be applied to the spectra before FFT to reduce side-lobes and improve image quality, but with a trade-off in slightly reduced axial resolution.
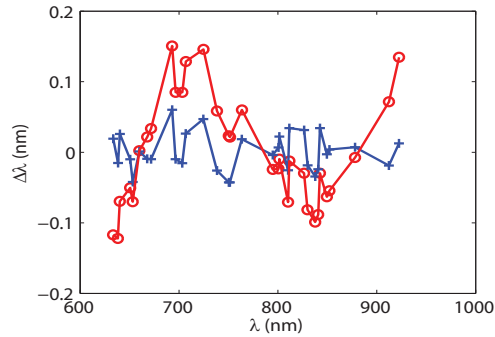
Fig. 2. Residual of fit to 31 Argon and Neon arc lines using the grating equation (red) and a 5th order polynomial (blue).

2.3 Instrument performance

The axial resolution of the system was measured with a glass microscope slide and found to be 1.8 μm in air (or 1.2 μm in varnish and paint assuming a refractive index of 1.5). Figure 3 shows that the measured axial resolution of 1.8 μm (in air) is close to the theoretical estimate of 1.7 μm (in air) from a simulation taking into account the actual spectrum of the source and the CCD spectral response. The highest sidelobes are 40 dB below the main peak (Fig. 4(b)), which can be reduced by applying a Hann window with a trade-off of reduced axial resolution of 2.2 μm in air. The transverse resolution was measured by scanning a USAF microscope chart and found to be 7 μm. Given that paint layers are fairly smooth, such a moderate transverse resolution is more than adequate and will not degrade the axial resolution. Figure 4 shows the OCT cross-section image and depth profile through a thin transparent layer of UV-cured epoxy resin (on a flat glass substrate) of a known thickness obtained from mechanical profilometry measurements. OCT measures the optical thickness of the resin to be ~4 μm which corresponds to ~2.6 μm in physical thickness (refractive index of the resin is ~1.53) consistent with the mechanical profilometer measured thickness of 2-3 μm.
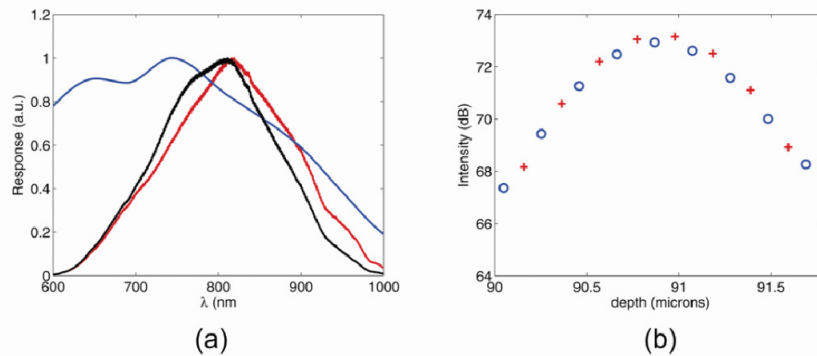

Fig. 3. Axial resolution of the UHR OCT. a) Spectrum of NKT SuperK Versa after spectral shaping at 810 nm (red), the spectrum of the CCD response (blue) and the source spectrum modified by the CCD spectral response (black); b) PSF simulated using the source spectrum and the CCD response (red cross) and the actual measured PSF using a glass slide (blue circle). The simulated spectrum was processed in the same way as the actual measured data.
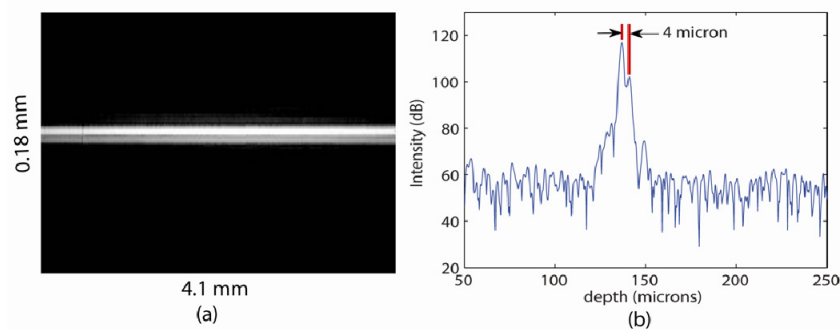
Fig. 4. UHR OCT imaging of a layer of UV-cured epoxy resin 2-3 microns (measured with a mechanical profilometer) deposited on a piece of glass. a) ultra-high resolution OCT cross-section image of the sample; b) depth profile (without any windowing function such as Hann window) showing the optical thickness of the resin to be 4 microns which corresponds to 2.6 microns in physical thickness (refractive index of the resin is ~1.53) consistent with the profilometer measured thickness of 2-3 microns.

Figure 5 shows the axial resolution measured from the FWHM of the depth profile of an air/glass interface as a function of depth. The axial resolution is constant around 2.2 µm (with Hann window) over a depth range of 1.5 mm using the more accurate wavelength calibration obtained through fitting a 5th order polynomial (see Section 2.2). However, if a slightly less accurate wavelength calibration (using the grating equation fit) is employed, the axial resolution increases with depth from 2.3 to 4.6 µm over the depth range of 1.5 mm. This example highlights the importance of accurate wavelength calibration.
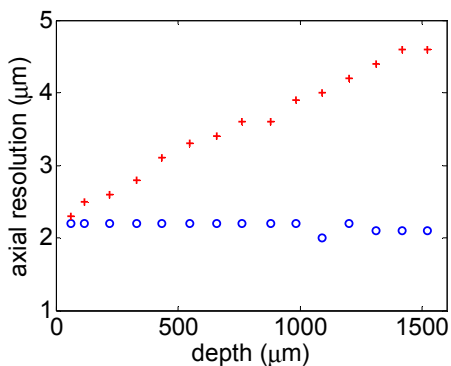

Fig. 5. Axial resolution as a function of depth using the 5th order polynomial (blue circles) and using the grating equation (red crosses) for wavelength calibration.

One of the problems with FDOCT is the drop in sensitivity with depth owing to finite spectral resolution with typical values of 10-20 dB mm^{-1}. A high spectral resolution spectrograph will reduce the sensitivity roll-off and increase the effective depth range. We have chosen a large array of 4096 pixels to ensure a high spectral resolution without compromising the large spectral range required for ultra-high axial resolution. For the best spectral resolution, the focused spot on the detector should be less than the pixel size. While the camera lens is designed for large format imaging (35 mm film) in the visible range, it is not optimized for the NIR range and noticeable chromatic focal shift in the 600-1000 nm range is observed. Keeping a good focus at the short wavelength end will result in a shorter effective central wavelength and better axial resolution. The fringe period (in pixels) for an interface at a given depth is smaller at the shorter wavelength than at longer wavelength which also means that it is more important to have good focus at the short wavelength end to

minimize sensitivity roll-off with depth. However, too much defocusing at the long wavelength end will also result in a reduction in spectral bandwidth. The camera lens focus was adjusted to give the greatest OCT depth range while maintaining high axial resolution. A He/Ne laser at 632 nm was coupled into the OCT and the width of the line at the detector was found to be less than one pixel showing that the focused spot on the detector was indeed less than one pixel at the short wavelength end. To measure the sensitivity roll-off with depth, the reference arm path length was varied while keeping the objective lens focused at the air/glass interface. The signal-to-noise ratio (SNR) in dB scale is defined as $20\log_{10}\dfrac{I_{peak}}{\sigma}$, where I_{Peak} is the peak intensity corresponding to the air/glass interface and σ is the noise estimated from the standard deviation of 500 repeat measurements of the intensity of a pixel 20 μm away from the peak position. Figure 6(a) shows the measured signal-to-noise ratio (SNR) in dB scale as a function of depth. The SNR varies within 2 dB over a 1.2 mm depth range which is largely consistent with the noise free theoretical simulation for our spectrometer setup assuming the spot size on the detector to be much smaller than the pixel size for the entire wavelength range. The sharp drop in SNR at 1.2 mm is as theoretically expected (assuming the spot size on the detector to be much smaller than the pixel size) due to the onset of aliasing which also shows that by keeping a good focus at the short wavelength end has resulted in near theoretical behavior despite the noticeable chromatic focal shift of the camera lens. The slight drop in SNR at low depth (<500 μm) is because of the increased noise at low depth. For example, Fig. 6(b) shows the reference-only noise derived from the standard deviation of 500 A-scans (in linear scale) at each depth. This increase of noise at low depth is found in other supercontinuum source based OCT [34]. The actual imaging range will depend on both the sensitivity roll-off due to the finite spectral resolution and the depth of field of the objective lens. While the sensitivity roll-off is 2 dB over a depth range of 1.2 mm, the current objective lens depth of field results in a drop of 2 dB over a range of ~0.1 mm which is sufficient for easel paintings but not wall paintings and other cultural objects such as ancient colored glass. However, since the layers are very smooth, an objective lens with 3-4 times the transverse resolution (i.e. 21-28 μm) will still be adequate and at the same time give an overall depth range of ~1.2 mm.

Visibility is maximized when the signal returned from the sample and reference arms are equal. Since the maximum reflectance that is likely to be encountered in a painting will be the surface of a varnish layer (only occasionally would we encounter a gold leaf) which has similar reflectivity as that of the surface of glass, the reference arm focusing module is connected to a fiber tip so that the intensity of returned signals from the two arms will be similar when imaging a strongly reflective surface on a painting. The signal to noise ratio is maximum when the integration time is adjusted such that maximum signal is just below detector saturation. This optimal integration time is 12 μs for an air/glass interface under an incident power of ~1.2 mW. To estimate the sensitivity of the system, a 6 mm thick glass slide was thus imaged at a depth of 500 μm and the peak intensity is found to be 72 dB above the noise floor in the absence of strong signals (i.e. measured by removing the sample). Since the reflectivity of the surface of the glass slide at normal incidence is ~4% which corresponds to 14 dB below a 100% reflective surface such as a mirror, the sensitivity of the system is therefore –86 dB. If data collection time is not a constraint, then averaging large number of frames can still reduce the noise significantly as shown in Fig. 6(c). Figure 6(d) shows that after ~4000 averages, the noise at a depth of 500-520 μm converges to a constant which is ~35 dB lower than that of a single measurement with no averaging. The noise level is estimated by taking the standard deviation of pixels in the 500-520 μm depth range from an averaged A-scan profile in linear scale. The reduction of noise as a function of the number of averages is proportional to the square root of the number of averages consistent with shot noise behavior. The maximum achievable sensitivity of the system is therefore –121 dB.

The camera readout speed is 37 kHz and typical optimal exposure time for paintings is 5-50 µs to avoid saturation. Hence, typical acquisition speed is 30 000 depth profiles per second, or a 3D volume is captured over a 5 × 5 mm² area in ~10 s with a transverse sampling interval of ~10 µm and incident power on the sample of ~1 mW. The OCT operates both in the online display mode and the fast capture mode, where, with the latter, once the region to be scanned is determined the system captures and saves the raw data to disk without post-processing thus speeding up the capture and data saving process which is the bottle neck in the absence of expensive servers. Automatic post-processing is done offline as a batch job to maximize the time spent on data collection. The focal plane of the objective lens is not flat. An image cube of a flat glass slide was imaged and the measured surface is used to correct for field curvature.
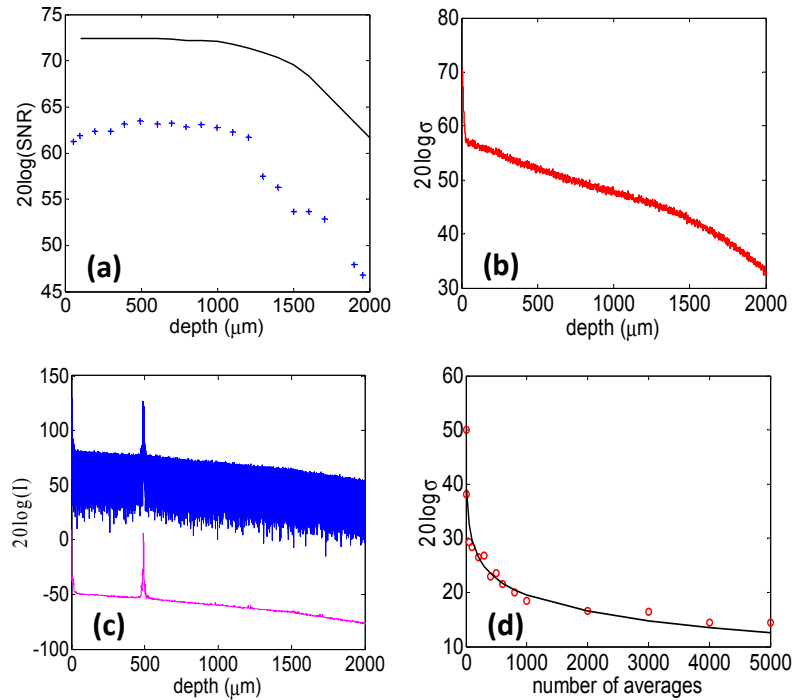
Fig. 6. Measurements of the UHR OCT sensitivity using a 6 mm thick glass slide: a) signal-to-noise measured as a function of depth while keeping the objective focus fixed on the sample surface (sensitivity roll-off) in blue crosses compared with the noise-free theoretical values (black curve) shifted down by 50 dB for clarity; b) noise with the sample removed as a function of depth calculated from 500 repeat measurements; c) a single A-scan (blue) compared with an average of 1000 A-scans (averaging was done in linear scale before converting to dB) shifted down by 100 dB for clarity (pink); d) noise measured at a depth of 500-520 µm (with the sample removed) as a function of the number of averaged A-scans (red circles) compared with expected shot noise behavior (black curve).

3. In situ UHR OCT imaging of an old master painting

Western European paintings in general have a varnish layer on the top surface for both the protection of the paint and for optical effects such that the paintings appear with better contrast and colour saturation. Most varnishes will degrade over time and become yellow and hazy. Conservators routinely remove old varnish layers and re-varnish paintings with new varnish. Sometimes, however, the old varnish layers are not completely removed, or paintings can be re-varnished without removing the older varnish at all, for example if a varnish has become slightly matt, especially after surface cleaning. A series of varnish layers might

therefore be found on a painting, applied at different times and reflecting the conservation history.

The UHR OCT was taken to the National Gallery in London to perform *in situ* imaging of a painting (Fig. 7(a)) chosen because it was known to have an accumulation of varnish layers of different thicknesses, and therefore was suitable for demonstrating the capabilities of the new OCT system. Figure 7(c) shows a cross-section image obtained with the UHR OCT at roughly the same position as that imaged with a commercial OCT (axial resolution of 6.5 µm in air and transverse resolution 9 µm) in Fig. 7(b). The UHR OCT image clearly resolves the thin varnish layer (layer 2) when it was barely resolved by the commercial FDOCT (~4 µm axial resolution in varnish). An actual sample was taken from this region, in the Virgin's cloak, and examined under a microscope, which confirmed the existence of a couple of varnish layers, beneath which is a blue paint containing mainly mineral azurite (basic copper carbonate). The cloak appears greenish overall because of the yellowed varnish obscuring the blue paint.
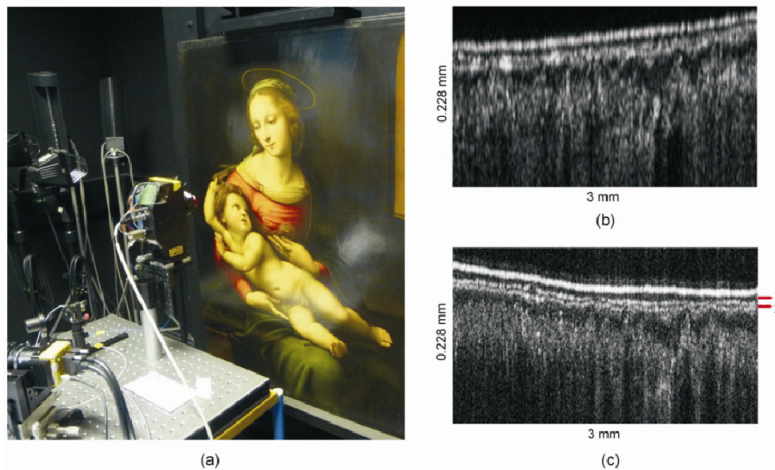

Fig. 7. Comparison of UHR OCT and commercial OCT images of roughly the same area on an old master painting. a) UHR OCT in situ imaging of The Madonna and Child (NG929, after Raphael, probably before 1600, © The National Gallery, London 2015) in the conservation studio of the National Gallery London; b) 930nm commercial OCT cross-section image of the Virgin's cloak; c) UHR OCT cross-section image at roughly the same position as a). The red bars to the right of the image indicates the top two varnish layers 1 and 2. The OCT images in b) and c) are of the same scale (3 mm wide by 0.228 mm deep).

Figure 8(a) shows a UHR OCT image in the region of the curtain in the background of the same painting towards the left edge, compared with an optical microscope image of a real paint sample prepared as a cross-section and viewed under visible light (Fig. 8(b)) and under UV light (Fig. 8(c)). The OCT image was taken next to the small sub-mm hole left by sampling. The sample shows that the curtain, which appears very dark because it is obscured by the yellowed varnish, is in fact green. The vertical scales of the two images are the same but the OCT image is not 1:1 in aspect ratio as the OCT image is more than 10 times wider than the real sample. In the microscope images of the real sample under visible and UV light, certain layers (e.g. layers 8,9,10 or layers 4,5,6) appear rather similar and difficult to delineate. The UHR OCT image not only resolves thin layer structures at a resolution comparable to the microscope image of a real cross-section, but also gives superior contrast allowing them to be more clearly distinguished. This is not surprising as OCT is most sensitive to refractive index discontinuities, which occur at layer interfaces, whereas normal colour images of real samples rely on the colour differences between layers.
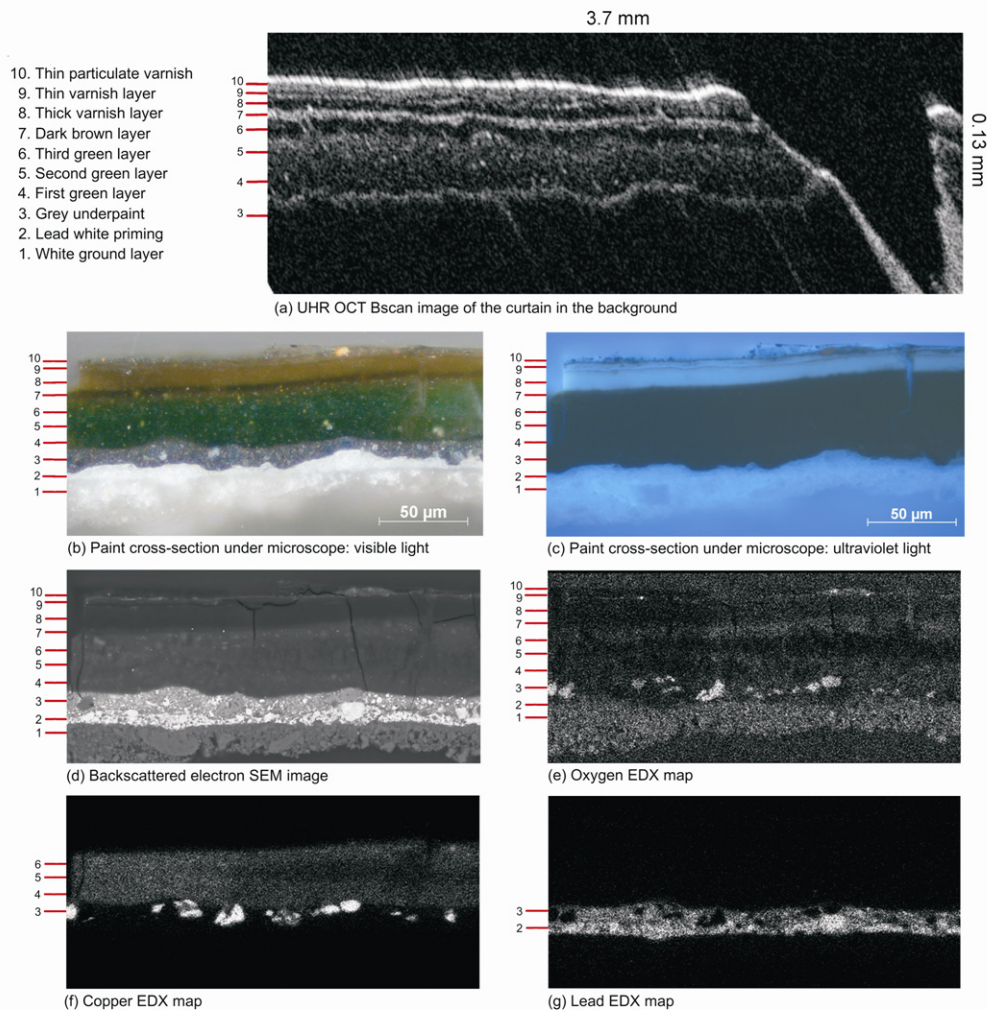
3.7 mm

10. Thin particulate varnish
9. Thin varnish layer
8. Thick varnish layer
7. Dark brown layer
6. Third green layer
5. Second green layer
4. First green layer
3. Grey underpaint
2. Lead white priming
1. White ground layer

0.13 mm

(a) UHR OCT Bscan image of the curtain in the background

(b) Paint cross-section under microscope: visible light

(c) Paint cross-section under microscope: ultraviolet light

(d) Backscattered electron SEM image

(e) Oxygen EDX map

(f) Copper EDX map

(g) Lead EDX map

Fig. 8. Comparison between UHR OCT 'virtual' cross-section image and microscope images of a sample taken from a nearby position on the painting in Fig. 6a. a) UHR OCT cross-section image of the background curtain, next to the position where a sample was taken (sample hole to the right of the image); two videos of an image cube around this region are given in Media 1 and Media 2; b-g) a paint sample from the curtain prepared as a cross-section and imaged under the optical microscope in visible and UV light and with SEM-EDX of the backscattered electron, oxygen, copper and lead (the scales of these images are identical). The vertical scale of the OCT image is ~130 microns after converting to physical thickness by assuming refractive indices of 1.5 for varnish and paint layers. The OCT image size is 3.7 mm in width which is different from the microscope images which are 0.24 mm in width. The microscope images in b-g have a 1:1 aspect ratio. The OCT image has been rotated to the same orientation as the microscope images (the optical axis was 4.5 degrees from the surface normal) and the bright diagonal stripes are artefacts because of the huge reflection from the shiny varnish at points where the varnish surface normal is exactly aligned with the optical axis.

In Fig. 8, the real cross-section shows (from bottom to top) a white chalk ground (labelled 1) and lead white priming layer (labelled 2). On top of these layers is a dark grey paint composed of lead white, azurite and black, which forms the underpaint for the curtain (layer 3). The OCT image only shows layers above this, as it has limited depth of penetration. To improve the penetration for highly opaque material (opaque due to scattering or absorption), long wavelength OCTs in the 2 μm wavelength regime have been developed within the

framework of the same project [35,36]. For the layers above, the UHR OCT not only allows the thinnest layers to be resolved, but also makes it easier to discern the features of the thicker layers and to make more detailed interpretations with greater confidence. For example, above the dark grey underpaint there are three green paint layers based on verdigris that are slightly different in composition (layers 4-6), just about visible in the visible light image at the far right of the cross-section, but more evident in the backscattered electron scanning electron microscope (SEM) image and the energy dispersive X-ray (EDX) maps showing the distribution of oxygen and copper. They are even more easily seen in the OCT image where the first layer appears fairly dark, the second lighter and more scattering and the uppermost green paint appears quite dark and transparent. An extremely thin low scattering layer with bright interfaces (labelled 7) can be seen in the OCT image at the surface of the paint (this layer is more obvious in the video provided in Media 1). It correlates with a layer in the visible light image of the paint cross-section around 3 μm thick that is darker than the layers above it, but which does nevertheless seem to be varnish rather than discoloration of the very top surface of the paint. There is some hint in the EDX map that some copper has migrated into this layer, which could have reacted with the varnish turning it a deeper brown. The next varnish layer is much thicker at around 9 μm (layer 8), with the SEM-EDX analysis showing there is dirt on top, giving a clear interface in the OCT image. This is followed by a very thin varnish (layer 9) and then a final layer containing particles (probably dirt) that is more scattering in the OCT image (layer 10). Table 1 gives a summary of the layer thicknesses as measured by OCT, optical microscopy and scanning electron microscopy. The OCT measured thickness (converted from optical thickness by assuming a refractive index of 1.5) agrees with those determined by microscopy.

Table 1. Layer thicknesses measured by OCT, Optical Microscopy (OM) and Scanning Electron Microscopy (SEM) [a]

Layers [b]	OCT [c] (μm)	OM (μm)	SEM (μm)
Layer 1: white ground layer	Not visible	Not measured [d]	Not measured
Layer 2: uneven lead white priming	Not visible	2–12	2–12
Layer 3: grey underpaint	>7 [e]	8–17	8–15
Layer 4: first green layer	10-17	9–13	9–14
Layer 5: second green layer	11-16	9–13	9–16
Layer 6: third green layer	8-11	8–12	7–12
Layer 7: dark brown layer	2-6	2–4	2–4
Layer 8: thick varnish layer	7-9	9–11	9–11
Layer 9: thin varnish layer	3-7	3–5	3–4
Layer 10: thin particulate varnish layer	3-5	3–6	2–5

[a]Measurements with OM and SEM were made on a paint sample prepared as a cross-section taken from an area adjacent to that imaged by OCT (Fig. 8). Thickness ranges are given since the paint layers are not uniform. Note that the paint cross-section is 0.55 mm in width but the area on the painting imaged by OCT is ~10 times larger.
[b]Layers are numbered from bottom to top as in Fig. 8.
[c]Optical thicknesses have been converted to physical thickness assuming a refractive index of 1.5.
[d]The white ground layer was not measured as the paint cross-section does not include its full thickness.
[e]OCT is not able to see the full layer as the grey underpaint absorbs light strongly.

7. Conclusion

In conclusion, an ultra-high resolution OCT at 810 nm has been developed for high depth resolution (~1.2 μm in varnish and paint) and high contrast imaging of varnish and paint layers for historical paintings. The fiber-based ultra-high resolution FDOCT achieved theoretical axial resolution through accurate wavelength calibration, while maintaining a constant axial resolution over a depth range of 1.5 mm and <2 dB in sensitivity roll-off within 1.2 mm depth range which makes a final imaging range of 1.2 mm possible using an objective lens that gives a transverse resolution of ~25 μm (the current objective lens gives a transverse

resolution of 7 μm which provides a depth range adequate for easel paintings). We have demonstrated that the UHR OCT, a non-invasive cross-section imaging technique, is capable of resolving very thin varnish layers on paintings at a resolution comparable to the conventional micro-destructive technique of imaging a real sample prepared as a cross-section. More importantly, the UHR OCT gives high contrast between layers that are difficult to distinguish in microscopy images of a sample prepared as a cross-section. The non-invasive nature of OCT, allows it to be used as an effective survey instrument for subsurface microstructure of paint and varnish layers prior to the application of complementary techniques for detailed chemical analysis, including decision for sampling if appropriate.

Acknowledgments